Growth and structural characterization of Fe_3O_4 and NiO thin films and superlattices grown by oxygen-plasma-assisted molecular-beam epitaxy

D. M. Lind, S. D. Berry, G. Chern, H. Mathias, and L. R. Testardi
Department of Physics, 315 Keen Building, B-159A, Florida State University, Tallahassee, Florida 32306-3016
and the Center for Materials Research and Technology (MARTECH), Florida State University, Tallahassee, Florida 32306-3016
(Received 13 May 1991)

Oriented single-crystalline thin films of NiO and Fe_3O_4, and Fe_3O_4/NiO superlattices have been grown on cleaved and polished substrates of MgO(001), using oxygen-plasma-assisted molecular-beam epitaxy. We report the growth mode and structural characterization of the grown films using *in situ* reflection high-energy electron diffraction (RHEED) and *ex situ* scanning electron microscopy and x-ray diffraction. The (001) surface of MgO provides an excellent template for the pseudomorphic growth of these thin films and superlattices, for it has a very small lattice mismatch (0.3–0.9 %) to the cubic rocksalt structure of NiO and to the half unit-cell dimension of the spinel structure of Fe_3O_4. Superlattices consisting of alternating layers of NiO and Fe_3O_4 have been grown with a repeat wavelength down to 20 Å (approximately one Fe_3O_4 unit cell plus two NiO unit cells) thick. These superlattices exhibit strong crystalline ordering and sharp interface formation. RHEED pattern evolution *in situ* during growth indicates formation of the rocksalt NiO crystalline symmetry and then the spinel Fe_3O_4 crystalline symmetry in a periodic sequence as each material is being deposited. Our data indicate single-phase crystal growth in registry with the substrate, with films of overall cubic symmetry. Strain in the grown films exhibits interesting effects that clearly do not follow a simple elastic model.

I. INTRODUCTION

Growth of high-quality single-crystalline thin films of metal oxides has become increasingly important recently for both technological and fundamental physical reasons. Ceramic oxides such as the ferrite spinels and magnetic garnets exhibit a rich complexity in magnetic coupling and electronic bonding not found in pure metallic and alloy materials. In addition, because of the strong anion-cation bonding in oxides, such films are often tribologically and chemically significant more stable than films with free metal or semiconducting surfaces. Oxide ferrites, especially those in layered structures, can also have superior magnetization and microwave resonance properties for use in a variety of planar device structures and other technological applications. Recently, the synthesis of layered oxide materials has received enhanced notoriety because of the discovery of high-temperature superconductivity in the ceramic perovskite oxides. As a result of this combination of factors, strong research interest deals with issues involved in the growth and integration of magnetic and superconducting oxide structures into planar integrated devices.[1–3]

Special emphasis in the research community is being focused on thin films and modulated structures of ferrite materials.[4–12] Magnetic spinels, for example, show great promise in planar device applications because of their superiority as high-density magnetic recording media, their resistance to corrosion and wear, and the inherent advantage non-"lossy" insulating ferrites have in microwave resonant circuits. In addition, layered structures of such ferrite materials allow controllable constraints to be placed on stoichiometry, lattice spacing, and strain that couple directly with their magnetic properties. As a result, layered magnetic oxides are ideally suited to a study of a number of fundamental issues dealing with magnetic coupling, ordering and anisotropy in nonitinerant electron magnetic systems. Using the preparation techniques of molecular-beam epitaxy (MBE), Bando and coworkers[4–9] have recently grown Fe_3O_4 films and Fe_3O_4/CoO superlattices, and, using reactive sputtering, Ortiz *et al.*[10,11] have grown Fe_3O_4 films and Yoshii *et al.*[12] have grown γ-Fe_2O_3 films. The current investigation extends these studies and demonstrates the ability to produce constrained metal-oxide thin-film stoichiometries, including modulated structures of high-crystalline order and purity with controllable magnetic ordering and properties.

In our work, highly oriented single-crystalline thin films of NiO, Fe_3O_4 and Fe_3O_4/NiO superlattices have been grown using oxygen-plasma-assisted MBE. We will discuss here the synthesis and characterization techniques used, with special emphasis on the crystal-growth techniques used and the structural characterization of the resultant films using reflection high-energy electron diffraction (RHEED), scanning electron microscopy (SEM), and x-ray diffraction (XRD). We have found the (001)-oriented surface of MgO single crystals to provide an excellent template for the pseudomorphic growth of both NiO and Fe_3O_4, for it has a small ($<1\%$) lattice mismatch to the cubic rocksalt structure of the former and to the half unit-cell dimension of the spinel structure of the latter. We report the preparation of NiO and Fe_3O_4 thin films, as well as superlattices consisting of al-

 ©1992 The American Physical Society

ternating layers of NiO and Fe_3O_4. The Fe_3O_4/NiO superlattices have been grown with modulation wavelength Λ between 20 and 258 Å (the lower limit being slightly greater than one Fe_3O_4 unit cell plus two NiO unit cells thick), with optimal crystalline order obtained at substrate growth temperature of 240 °C. These films exhibit coherent single-crystalline ordering over several hundred repeat wavelengths. Reported elsewhere in the literature are studies we have made on the magnetization and electron transport properties of these thin films and superlattices[13–15] which show such effects as an unusually large in-plane versus out-of-plane anisotropy ($> 10^6$ difference) in electron transport as well as strong modulation wavelength-dependent magnetic ordering effects.

Motivation of lattice match and structure

The crystallographic structure of MgO, NiO, and Fe_3O_4 all have cubic symmetry and are based on a face-centered-cubic (fcc) oxygen sublattice. In MgO and NiO the overall crystalline configuration is the NaCl or "rocksalt" crystalline structure where a cut through the (001) plane is shown in Fig. 1(a). In this structure, oxygen ions and metal ions each form a close-packed fcc sublattice, with each oxygen ion surrounded by an octahedral pattern of six nearest-neighbor metal ions and vice versa.

Fe_3O_4 has the spinel crystal structure,[16] shown in Fig. 1(b), in which the oxygen ions form a fcc lattice, but with the iron ions taking up interstitial positions such that $\frac{2}{3}$ of them fill octahedral sites around each of the oxygen ions as in the rocksalt structure. The other third of the iron ions occupy tetrahedrally coordinated interstitial sites, each surrounded by four oxygen ions. This arrangement gives an Fe_3O_4 spinel structure with twice the unit-cell dimensions of the rocksalt unit cell. The crystallographic unit-cell edge dimensions for MgO, NiO and Fe_3O_4, as reported in the literature,[17] are 4.212, 4.1760, and 8.3976 Å, respectively, corresponding to an average interatomic layer spacing (oxygen-to-oxygen spacing along a ⟨001⟩ direction) of 2.1060, 2.0880, and 2.0994 Å for each of these lattices, respectively. This gives a lattice mismatch between MgO and NiO that is 0.86%, between MgO and Fe_3O_4 that is 0.31%, and between NiO and Fe_3O_4 that is 0.55%, thus providing a good epitaxial growth template for any one of these materials on any one of the others.[18,19] The fractional difference in lattice spacing, between the spinel unit-cell dimensions of Fe_3O_4 structure and the NiO and MgO rocksalt crystal structures, is due to the difference in the ionic radii and positioning of the metallic ions. Recent theoretical work[20] indicates that when anharmonic contributions are included, the strain at the interfaces is accommodated more easily in a growing film under conditions of slight expansion from the natural film lattice parameter rather than under conditions of compression. Therefore pseudomorphic layer-by-layer growth would be expected more readily for growth of NiO and Fe_3O_4 on substrates of MgO, rather than vice versa, because MgO has a slightly larger lattice constant than either of the other two materials. In addition, these materials cleave readily along {100} surfaces, and thus the MgO(001) crystallographic plane was chosen as the substrate for all of the film growths described here.

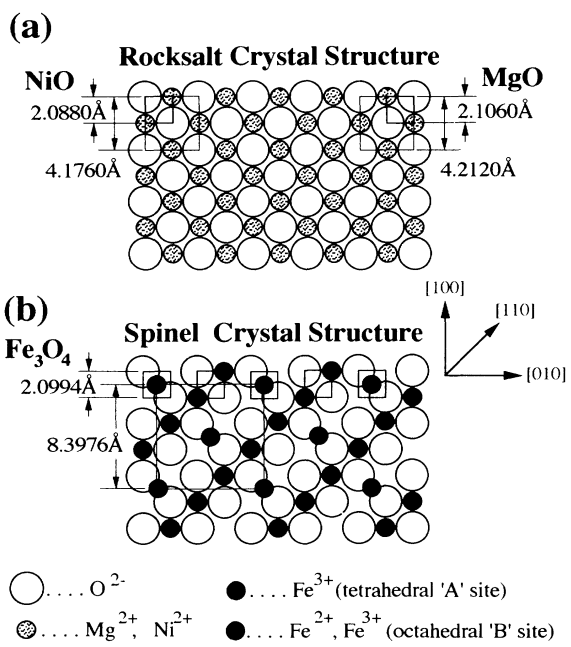

FIG. 1. The surface net of the (001) face of NiO, MgO, and Fe_3O_4. The overall symmetry is that of a face-centered-cubic oxygen lattice with metal ions coordinated around the oxygen sites. The spinel structure has two different Fe coordination sites, either octahedrally and tetrahedrally coordinated about alternating oxygen sites. The tetrahedrally coordinated sites shown lie $\frac{1}{2}$ lattice plane in front of the plane in which the rest of the atoms lie. The MgO and NiO structures have the NaCl (rocksalt) -structure crystal symmetry.

II. THIN FILM AND SUPERLATTICE CRYSTAL GROWTH

Physical apparatus and technique

Our samples were grown in the UHV MBE vacuum chamber[21] shown schematically in Fig. 2. The vacuum vessel is divided into two separate turbomolecular-pumped vacuum chambers connected with a 8.0 in. i.d. gate valve. The upper or "substrate" chamber has facilities for sample heating between ambient and 1100 °C, RHEED electron diffraction, film deposition rate monitoring, and residual gas analysis. The lower, or "source," chamber contains the molecular-beam sources for deposition of materials onto the substrate surface, and includes four EPI Systems Knudsen-type effusion sources, dual Temescal 15-kW electron-beam evaporation sources, and a Wavemat electron-cyclotron resonance (ECR) microwave plasma ion source, each oriented so that their effusion beam axis is directed toward the substrate growth position. Each of the deposition sources in this configuration has a source-to-substrate distance of 12.0 in. and is electropneumatically shuttered, with feedback control for shuttering based on monitoring of the deposit-

ed film thickness. The typical base-pressure achievable after appropriate baking to 200 °C in both chambers is below 1×10^{-9} Torr. With controlled oxygen flow and plasma generation during growth, the pressure is in the range of $2-3\times10^{-6}$ Torr, with the [residual gas analysis (RGA) measured] background partial pressures of all gases other than O^+ at 16 amu and $O_2{}^+$ at 32 amu below 1×10^{-10} Torr.

The geometry of the deposition is such that a quartz crystal microbalance detector head, situated immediately adjacent to the substrate during growth, has the same direct line of site to the deposition sources as the substrate. Depositing flux to the substate may be blocked using a manual shutter in the upper chamber, while the incident flux from any one or the sum of all of the deposition sources is being monitored. Shuttered line-of-sight viewports to each of the deposition sources are also available for periodic monitoring of the source material in each of the cells.

The MgO(001) substrates used for growth were commercially obtained 5×10 mm^2 single crystals 0.5 mm thick, which had been cut to within $\pm1.0°$ of the crystallographic (001) plane and polished to $\frac{1}{4}$-μm surface finish.[22] The substrates were triple rinsed in trichloroethylene, acetone, and methanol before insertion into vacuum. For growth, the substrates were mounted on the downward facing front plane of a molybdenum sample transfer puck situated within a resistively heated sample heating shroud. Substrate face temperatures are externally controlled using proportional-integral-differential (PID) feedback control over the range 30 °C–1100 °C and are repeatable under all configurations of thermal loading to within ±3.0 °C with thermal stability during the run to within ±1.0 °C. The substrate surface is cleaned *in situ* by heating to 600 °C for 10–30 min. After cleaning, the sample temperature is lowered to the growth temperature of 240 °C, and left to soak for at least 60 min. Samples thus prepared are found, independently by x-ray photoemission and electron diffraction, to be atomically clean to within a half percent of a monolayer and having good surface crystalline order.

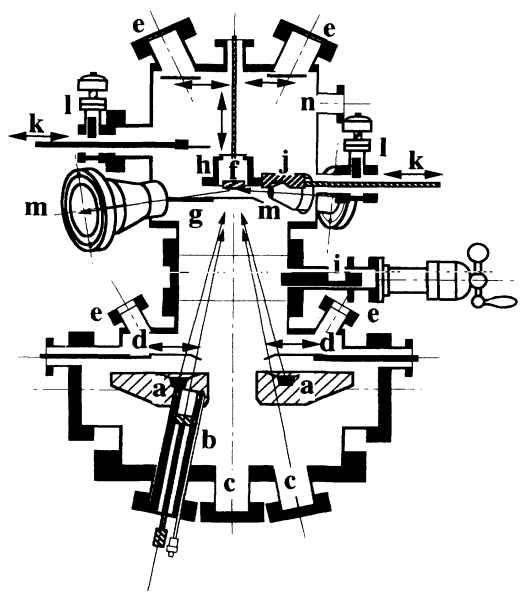

FIG. 2. Ultrahigh vacuum molecular-beam epitaxy (MBE) thin-film growth chamber. The deposition sources are in the lower chamber facing upward and include two 15-kW electron-gun sources (*a*), an ECR magnetically focused gas plasma source (*b*) with gas inlet, and four Knudsen effusion sources [not shown (*c*)], with all sources pneumatically shuttered (*d*), and source charges visible from shuttered viewports (*e*). The substrate holder (*f*) is shuttered (*g*) and placed in a heating shroud (*h*) in the upper chamber. The chambers are joined by an 8.0-in. i.d. isolation gate valve (*i*). Both quartz crystal deposition rate monitor head (*j*) and the substrate holder (*f*) may be retracted (*k*) and gated (*l*) from the main chamber for replacement. Grazing incidence RHEED diffraction (*m*), and quadrapole residual gas analysis (*n*) are also available in the upper chamber.

X-ray, RHEED, and SEM studies indicate that single thick layers of Fe_3O_4 and NiO grow to proper stoichiometry under slightly different conditions. The growth of NiO thick films (from a few monolayers all the way up to several micrometers thick) are accompanied by sharp RHEED, single-crystalline XRD patterns, and near-atomically flat surfaces and seen under SEM, for substrate temperatures from room temperature up to approximately 250 °C–260 °C. Under such conditions NiO will grow as a single-crystal rocksalt structure with (001) film planes oriented in alignment with the (001) planes of the substrate. Above that temperature, the RHEED patterns degrade sharply with rings rather than diffraction lattice rods, SEM patterns indicate very jumbled, rough surfaces, and XRD patterns contain diffraction peaks associated with nickel oxide growth that is polycrystalline and randomly oriented. The growth of Fe_3O_4 films has been evaluated over the range from room temperature to 450 °C, and it is found that the Fe_3O_4 stoichiometry, with the spinel structure oriented in alignment with the substrate lattice, is obtained for growth at or above approximately 225 °C, with polycrystallinity and multiphase growth evident in the RHEED, SEM, and XRD data for growth below that temperature. The x-ray data for room-temperature growths of thick iron oxide films include diffraction lines associated with randomly oriented microcrystallites of the bcc α-Fe iron and α-Fe_2O_3 hematite. As a result of the narrow overlap of good NiO and Fe_3O_4 growth temperatures, all of the superlattices reported here were grown at a substrate temperature of 240 °C. This growth temperature happens to fall well below the magnetic ordering temperature of Fe_3O_4 and very nearly the Néel temperature of NiO, although no special importance is placed on the proximity to the NiO Néel temperature. We have strong indications that, especially for the thinnest layered superlattices, the strain within the growing layers allows for some relaxation of the narrow temperature growth window, but for the present study we have not explored in detail all the parametric space (temperature, deposition rate, plasma density, etc.) that might provide satisfactory growth conditions for our superlattice structures.

The atomic flux deposited to form the Fe_3O_4 and NiO layers was introduced as pure metallic Fe and Ni from

two Temescal electron-beam evaporation sources and O^+ free radicals from a Wavemet microwave/ECR plasma generator. The plasma source, situated 12.0 in. from the substrate surface with plasma emission axis directed toward the substrate, provides a flux of oxygen with a high ionization percentage using the evanescent microwave intensity from a quartz window-terminated microwave cavity. A confining magnetic field from a permanent magnet, mounted in the nose of the plasma source, creates electron cyclotron resonance that enhances plasma production, and also acts to focus the plasma flux towards the substrate.

During our growth, high-purity O_2 was metered into the chamber, initially to a pressure of 8.5×10^{-5} Torr, through a needle valve that feeds the gas into an annular ring into the region immediately in front of the quartz window that makes up the front face of the microwave cavity. A microwave power of 250 W is delivered to the microwave cavity, and the resonant volume is then tuned to minimize the reflected power (to ~25–40 W). Under such conditions, the plasma discharge is clearly visible as a whitish torus in the region immediately in front of the quartz window. While codepositing O^+ and Fe, the plasma torus becomes a striking greenish color. The codeposition of Fe and O^+ plasma appears to lower the total pressure in both the upper and lower chambers by approximately an order of magnitude (as monitored by inverted magnetron, ionization gauging, or quadrapole mass spectrometry), probably due to strong gettering of the ambient gas by newly deposited iron on the chamber walls. Stable film growth at Fe_3O_4 and NiO oxygen stoichiometry is obtained whenever the plasma is visibly "lit," down to reasonably low vapor pressures. It is, however, very difficult to maintain plasma stability at apparent chamber pressures below approximately 1.0×10^{-5} Torr, and thus the pressure is maintained between 1.5 and 3.0×10^{-5} Torr during growth. Even at these pressures we are working at a moderate oxygen overpressure for growth. Studies are now underway to test the utility of mixed inlet gases ($Ar+O_2$) in lowering the reactive gas pressure while maintaining plasma stability and conserving proper Fe_3O_4 stoichiometry. Residual gas analysis indicates a significant enhancement of O^+ (16 amu) partial pressure compared O_2^+ (32 amu) with the plasma lit. Reports of growth of similar metal oxide films in the literature, by Bando and co-workers,[4–7] where the oxygen flux for deposition was provided by flowing O_2 through the chamber, indicated that oxygen vapor pressures and order of magnitude higher [$>(1-2)\times10^{-4}$ Torr] were required for growth at proper stoichiometry. Our results indicate that the more reactive oxygen plasma-assisted growth allows the total pressure during growth to be reduced significantly below those levels reported earlier.

High-purity (>99.99%) Fe and Ni source material[23] was premelted into a molten pool *in situ* in the water-cooled Temescal electron-gun source hearth under UHV, using an electromagnetically rastered 7–9-kV electron beam from the Temescal electron-gun filament source. Typical electron emission current and beam energy for heating and melting the source materials during deposition were 0.08–0.13 A and 8 kV from each of the sources, which provide a precisely controllable deposited metal flux to the substrate between 2.0–2.5 Å/sec. During a typical deposition run, the flux rate from each source was found to be very stable, with slow long-period drifts that could be monitored and maintained manually to within ±(5–10)% over the period of 1 h, which is required to deposit a typical 1-μm-thick film. The flux incident at the substrate position (actually the total metal oxide deposited) was monitored and used during superlattice growth to control the shuttering of the individual sources.

During growth, every effort has been made to minimize source conditions that alter or degrade the deposited film quality. Without careful control, the surfaces of the metal sources will oxidize heavily during use and crust over, and the sources (especially the Ni source) will tend to spurt metallic clusters that will be incorporated into the deposited flux. This spurting is found especially at higher flux rates and under conditions where the source pool within the electron-gun hearth is not completely premelted. It is therefore important (1) during the setup before deposition to carefully premelt the entire surface of source pool, and (2) to deposit films at moderate to low flux rates using the largest rastered molten source pool surface area possible. These precautionary steps provide a large thermally uniform emissive surface, and thus uniform deposition rates, and also act to self-clean the sources.

During superlattice growth, the deposited flux onto the substrate is alternated between nickel oxide deposition and iron oxide deposition by sequentially shuttering open and closed the nickel and iron sources. The automatic control of this shuttering is directed by monitoring the accumulated metal oxide mass added to the surface of the quartz crystal oscillator sitting immediately adjacent to the substrate. The differences between the two metal oxide densities and tooling factors, as well as the differences between deposition geometry of the substrate and quartz oscillator head, are accounted for by using the densities and total deposited layer thicknesses from a series metal oxide film calibration growths. The depositing flux rate and total deposited layer thickness on the substrate can be monitored and adjusted with a sensitivity of ±0.1 Å/sec and ±1.0 Å, respectively, and the feedback and shuttering mechanism have a "reaction time" of approximately 250 msec. Using present methods of monitoring deposited flux as the layer thickness feedback parameter gives an idealized total-layer-thickness control and repeatability of within ±1 Å.

The limiting factor in layer thickness control during growth is the thermal response of the quartz crystal oscillator. As the deposition monitor crystal is repeatedly exposed to varying thermal loading as alternating deposition source shutters are opened and closed, changes in the quartz crystal elastic modulus cause a sharp temporary increase or decrease in the crystal deposition rate monitor oscillation rate to be seen. This spurious rate transient is an artifact of the sharp thermal loading changes and not of any real changes in the depositing flux rate, and decays exponentially back to the "real" flux rate

as the monitor head returns to thermal equilibrium in approximately 3–4 sec. The effect of this flux rate transient appears in the grown layers as a deposited thickness offset and limits precise total thickness control to ±2–3 Å. Clearly, such difficulties affect the layered structure growth most severely for superlattices with the shortest modulation wavelengths. Real-time modeling and compensation for the thermal transients, incorporated into the substrate shutter control, would allow for nearly exact compensation of these thermal transients, and should provide subangstrom layer thickness shuttering control. Work is underway to incorporate such changes into our system at this time. On the other hand, because the apparent flux transients are seen at the beginning of *every* layer deposited, layer thickness repeatability is not strongly affected, and layer coherence in the grown superlattices can readily be held to within ±0.5 Å. XRD rocking curve measurements of the superlattice satellite peaks, which are a sensitive measurement of the layer coherence, support this level of layer thickness repeatability.

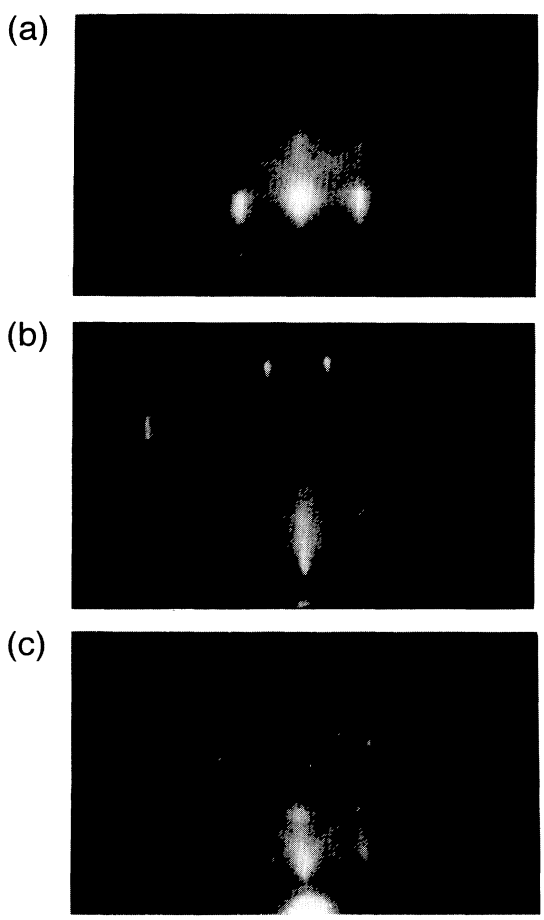

FIG. 3. RHEED images of (a) MgO(001), (b) NiO/MgO(001), and (c) Fe_3O_4/MgO(001), taken at 10 kV along a ⟨100⟩ azimuth. The images are seen as though scattering off a crystal facing upward. See text for discussion.

III. EXPERIMENTAL RESULTS

A. *In situ* RHEED characterization

RHEED diffraction patterns, taken during deposition of the thin films, and superlattices reflect the two-dimensional surface net and give insight into the growth mode and crystallographic order at the surface. Figure 3 shows the RHEED patterns from (a) a clean MgO(001) substrate, (b) a NiO-terminated film, and (c) a Fe_3O_4-terminated film, each grown at 240 °C, with each diffraction pattern taken such that the 10-kV electron beam is incident at approximately 1° scattering angle along the ⟨100⟩ azimuth. The diffraction pattern for MgO, shown in Fig. 3(a), shows vertical lattice rods and radial Kikuchi lines indicative of a well-ordered and reasonably flat surface. The diffraction pattern in Fig. 3(b), from a typical NiO surface, is very similar to that of the substrate on which it is grown, shown in Fig. 3(a). The lattice rods have essentially the same angular separation for NiO as for MgO, indicating that the in-plane lattice spacing, orientation, and overall crystalline quality in the two structures are essentially the same. (The ≤1% difference expected in lattice spacing between these two structures is too small to distinguish in the RHEED patterns.) In both diffraction patterns radial Kikuchi lines, indicative of good near-surface three-dimensional crystalline order, are also present. Some differences may be noted, however. The NiO diffraction pattern shows a ring of very sharp, short, secondary diffraction rods from the first Laue diffraction zone in the upper part of the image, that are only barely discernible in the diffraction pattern from the MgO surface, and in the NiO diffraction pattern the lattice rods have sharpened up slightly, indicative of small improvements in surface flatness and long-range coherence.

The diffraction pattern in Fig. 3(c) from a typical Fe_3O_4-terminated surface show, in addition to the RHEED streaks reflective of the overall fcc repeat spacing which are at the same angular spacing as in the MgO and NiO patterns, half-order streaks that reflect the coherence from the longer spinel unit-cell periodicity. The latter is twice the repeat distance in real space as the underlying fcc oxygen lattice, causing the additional fractional order diffraction streaks to fall at half the angular separation of those seen above. The Fe_3O_4 diffraction pattern also exhibits a ring of secondary diffraction rods from a closer-in half-order Laue diffraction zone. A second much dimmer ring of diffraction points from the first diffraction zone are visible at the upper edge of the field of view, at the same angular radius as the diffraction ring of spots seen in NiO RHEED diffraction. These additional features—the half-width-spaced lattice rods and the inner secondary ring, taken together—are equivalent to half-order diffraction spots observable in low-energy electron diffraction for surfaces that are reconstructed or have a long-range super-periodicity, and are clear evidence for the formation of the spinel structure which has twice the real-space length periodicity of the rocksalt structure. The same type of surface lattice coherence and half-order periodicity for Fe_3O_4 is also seen for RHEED

taken along other high-symmetry diffraction directions.

The appearance and disappearance of the more complex spinel RHEED pattern and the simpler rocksalt RHEED pattern, as a growing superlattice alternates between Fe_3O_4 and NiO growth, can be used to quantify the rate at which the crystalline ordering evolves from the rocksalt structure to the spinel structure, and vice versa, during superlattice deposition. When shuttering the sources from Fe_3O_4 deposition to NiO deposition, the observed diffraction pattern is seen to evolve very rapidly from the spinel pattern to the rocksalt pattern—in roughly a second after shutter opening. Evolution of the observed diffraction pattern from the rocksalt to the spinel pattern, when shuttering from NiO deposition to Fe_3O_4 deposition, does not occur as rapidly after shutter opening, but is clearly evident within 4–5 sec. This is approximately the time it takes to deposit between four and six atomic layers—roughly $1-1\frac{1}{2}$ iron oxide spinel unit-cell depths. The spinel diffraction pattern continues to sharpen up during growth for approximately 8–10 sec after shutter opening, until the image shown in Fig. 3(c) is seen. This diffraction pattern is essentially identical to that seen whether the Fe_3O_4 layer is 10–15 or 5000 Å thick. The sharp transitions from spinel Fe_3O_4 growth to rocksalt NiO growth is a strong indication that abrupt interfaces are being formed during growth. Their occurrence, however, is not a sufficient condition for the presence of abrupt interfaces in the final superlattices, because subsequent bulk interdiffusion could take place that could potentially give large compositionally graded interface regions. *Ex situ* x-ray diffraction analysis after growth of our films, to be discussed below, indicates, however, that very little interdiffusion takes place in our superlattices. In addition to the alternation between the two crystallographic diffraction patterns during layered structure growth, visual observation and early quantitative measurements show clearly the presence of RHEED intensity oscillations that correspond to the atomic-layer-by-atomic-layer deposition of each of the constituent materials. Work is now underway to further study these RHEED oscillations.

B. Structural analysis by x-ray diffraction and SEM

X-ray diffraction studies have been performed on the NiO and Fe_3O_4 films, grown on MgO(001), using a Siemens 2θ-θ coupled D-500 diffractometer with θ-offset capability for use in cases where the crystal mounting base (or surface) and the crystallographic planes are not parallel. Cu radiation was used, giving x-ray $K\alpha_1$ and $K\alpha_2$ lines at 1.540 60 and 1.544 43 Å, respectively. A graphite post monochromatic eliminates all other wavelengths from the detected intensity, and collimating slits limit angular divergence to 0.1°, with analyzer collimating aperture set at 0.05°, setting the angular resolution.

We report here three types of angular scans that are obtained for our samples: (1) using the mode of coupled scanning with the possibility of θ offset—called hereafter "θ-2θ" scans—in which the θ and 2θ motions are swept together, which are used to obtain the crystallographic interlayer spacings as well as the superlattice modulation wavelengths; (2) utilizing the mode of scanning the 2θ detector position through the intensity maximum while holding the θ motion, which sets the sample position, fixed—hereafter "2θ-rocking" scans—after optimizing at diffraction peak peak position. The angular full width at half maximum (FWHM) intensity of these scans give a measure of the interlayer or modulation wavelength coherence, depending on the particular diffraction peak being scanned. (3) "θ-rocking" scans—in which the 2θ detector position is optimized on a diffraction peak position and then held fixed, while the θ sample orientation motion is rocked through the intensity maximum. The FWHM of these scans gives a weighted summation over all those sample orientations for which the Bragg reflection conditions are met, and is a measure of the mosaic spread in the films due to small-angle twinning or other mechanisms.[24–26]

Coupled θ-2θ x-ray diffraction scans have been taken for each of our samples covering a range in 2θ from near zero to near 105°. In each of the diffraction patterns, sharp high-intensity peaks are observed near $2\theta=42°-44°$ and 94°–95°, which for MgO and NiO correspond to the d_{002} and d_{004} spacings, and for Fe_3O_4 correspond to the d_{008} and d_{004} spacings, respectively.[27] For diffraction from superlattices, satellite or "sideband" peaks are seen on the high- and low-angle sides of each interlayer spacing diffraction peak. In addition small "contaminant" features are seen in the spectra from some of the films. A small broad feature (FWHM $\geq 2.0°$) is observed near $2\theta=52°$ for diffraction from a few of the films. This feature corresponds to the (002) peak from microcrystalline nickel incorporated into the film by spurting from the nickel electron-gun source. The total integrated intensity of this microcrystalline nickel feature, when present, is $\leq 2\%$ that of the (002) of the NiO or superlattice central diffraction feature near $2\theta=43.3°$. Also present in the spectra from most samples is a very small feature near $2\theta=38°$ associated with the aluminum mounting plate used in the x-ray diffractometer. No other features with total integrated intensity greater that 0.1% that of the main film peaks are observed in any of the spectra.

Figures 4(a)–4(c) present the portion of the θ-2θ diffraction scans in the range near $2\theta=94°-95°$ for a typical polished MgO substrate, for an NiO film, and for an Fe_3O_4 film (each approximately 1 μm thick and grown at 240 °C substrate temperature and a 2.0-Å/sec deposition rate). These spectra show the (004) diffraction peaks for MgO and NiO, as well as the (008) diffraction peak for Fe_3O_4.[27] Figure 4(d) shows the comparable diffraction features for one of our grown superlattices, with the superlattice chosen having modulation wavelength $\Lambda=64.8$ Å, with 131 bilayer repeats, and with 29.4 Å Fe_3O_4 layers and 35.4 Å NiO layers. Superimposed on this last spectrum is a vertically expanded version of the same profile magnified 20 times to show the ± 1 sideband features. The angular spacing of the sidebands is used to measure the modulation wavelength of each of the superlattices. The particular angular range shown in the figure is chosen because the peaks from each of the respective diffraction features are seen clearly with little overlap. Although only a narrow angular range of the measured

diffraction pattern is shown, essentially all of the important features can be seen. Each diffraction peak in the spectra is seen as a doublet, with the $K\alpha_1$ line at lower angle and the $K\alpha_2$ line at slightly higher angle and one-half the $K\alpha_1$ peak intensity. Typically, the x-ray diffraction features are sharp, high intensity ($>10^4$ counts/sec) peaks with very low background count rates ($<1-5$ counts/sec). The peak positions are reproducible to within $\pm 0.017°$, giving a statistical interlayer spacing uncertainty of ± 0.0008 Å or 0.04%. All interatomic layer spacings reported here are for spacings between oxygen planes in the (often slightly distorted) underlying fcc crystalline structure, measured normal to the grown film plane.

The only features observed in the x-ray diffraction pattern from the MgO substrate are the MgO(002) and MgO(004) reflections at $2\theta(K\alpha_1)=42.949°$ and 94.135°, respectively, and the latter is shown clearly as a $K\alpha_1/K\alpha_2$ doublet in Fig. 4(a). This indicates that the surface normal for the cut face of the bulk solid is along the [001] direction with an interatomic layer spacing of 2.1042 Å. X-ray 2θ-fixed, θ-rocking diffraction spectra for MgO gives a mosaic spread (FWHM) in the substrate of 0.120°. θ-fixed, 2θ-rocking x-ray diffraction measurements, which are reflective of the interatomic layer coherence, give a FWHM linewidth of 0.062°. If we take the angular resolution of the diffractometer to be 0.050° (probably a lower limit), removal of the instrumental resolution gives the maximum contribution to the linewidth from variation in lattice parameter as 0.037°,

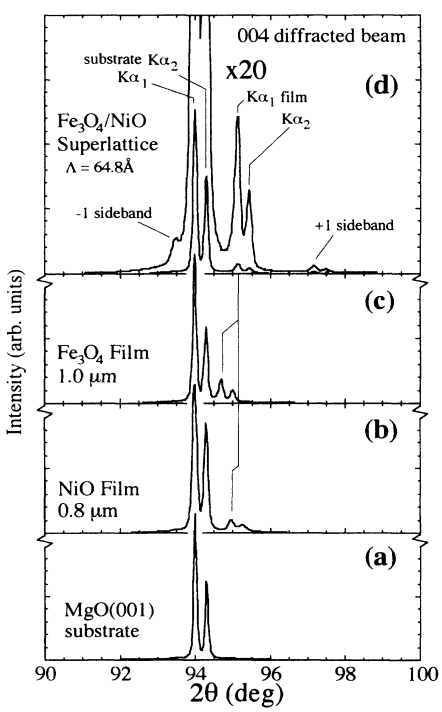

FIG. 4. X-ray diffraction spectra from (a) MgO(001) substrate, (b) 0.8-μm-thick NiO/MgO(001) film, (c) 1.0-μm-thick Fe_3O_4/MgO(001) film, and (d) [Fe_3O_4(29 Å)]/[MgO(35 Å)] superlattice, in the vicinity of the substrate (004) diffraction line. See text for discussion.

corresponding to a lattice coherence of ± 0.0008 Å or 0.04% of an interatomic layer spacing. Because the linewidth here is very nearly the angular resolution of the instrument, we believe this represents a high degree of uniformity in the interlayer spacing.

The interatomic layer spacing of the iron oxide and nickel oxide layers in the grown films have equilibrium lattice spacings that are slightly smaller than that of the MgO substrate and thus would be expected to have diffraction peaks close to, but slightly higher in angle than, the substrate peaks. The NiO x-ray diffraction pattern, with the (004) peaks shown in Fig. 4(b), shows alongside the substrate diffraction lines, diffraction lines at $2\theta(K\alpha_1)=43.291°$ and 95.015° associated with the NiO(002) and NiO(004) lattices, respectively. These peaks indicate an underlying fcc lattice with interatomic layer spacing of 2.0883 Å. This lattice spacing is essentially identical to that reported in the literature. As noted above, no other features are observed in the spectra between $2\theta(K\alpha_1)=1°$ and 105°, and their absence indicates oriented growth along a $\langle 001 \rangle$ axis nearly parallel to the (001) MgO crystallographic axis.

It is interesting to note that for these NiO films, as well as for the Fe_3O_4 films and superlattices, the substrate and film axes do not appear to be precisely aligned. The diffractometer alignment used to optimize for maximum diffraction peak count rates for the film peaks are at a small θ offset (approximately 0.30°) from the alignment for optimal substrate peak maxima. This angular offset does not appear to be an artifact to the θ-2θ diffractometer alignment itself, because other tests of that alignment, including the rocking measurements for superlattice coherence, would preclude it. The angular offset rather appears to be a result of small crystallographic axis differences between the film and substrate. It is not known whether these are a result of strain-relieving distortions in the film or simply due to the small cut misalignment between crystallographic and surface normal directions in the polished substrate surface. However, Van der Merwe[28,29] has noted that such deviations between the substrate and film crystallographic planes have been observed for other systems and are thought to be a compensation mechanism for accommodating misfit at the interface.

X-ray, RHEED, and SEM data indicate good single-crystalline growth. X-ray rocking curve data for NiO indicate mosaic spread within the film of 0.330° (θ FWHM) and layer spacing coherence of ± 0.0019 Å(2θ FWHM angular width of 0.083°). SEM images of these films taken with a JEOL JXA-840A electron probe microanalyzer in secondary electron mode appear flat and featureless down to the resolution limit of the instrument, except for tiny amounts of dust deposited on the surface, which effectively act as a resolution target. Such images indicate a growth mode that ends with a very flat surface, and is consistent with layer-by-layer single-crystal growth. Similar unusually flat surfaces are seen in the growth of the short-wavelength ($\Lambda \leq 65$ Å) superlattices and for some of the Fe_3O_4 films. SEM images of films that have been cracked or scribed also indicate that cleavage planes within the film line up with the {100}

crystallographic planes of the substrate.

The Fe_3O_4 diffraction spectra obtained show, superimposed and partially overlapping the substrate peaks, diffraction peaks reflecting the Fe_3O_4 interatomic layer spacings at $2\theta=43.176°$ and 94.732°, the latter shown in Fig. 4(c). The observed peaks correspond to the spinel unit-cell (004) and (008) diffraction layer spacing and reflect a (001) orientation in film growth with interatomic layer spacing of 2.0935 Å. This interatomic layer spacing is 0.27% smaller than the equilibrium lattice spacing of the cubic bulk Fe_3O_4 reported in the literature.[17] No other diffraction lines are observed in the spectra, indicating the absence of multiple-phase formation, or of multiple growth orientations in the deposition of these films. X-ray rocking curve data indicate mosaic spread within the Fe_3O_4 film of 0.174° (θ FWHM) and layer spacing coherence of 0.0011 Å (θ FWHM angular width of 0.069°)—each of these being smaller than the comparable linewidths for NiO and very nearly that of the underlying MgO lattice.

SEM images of these films present somewhat mixed results. Some of the Fe_3O_4 films grown appear to be formed of columnar growth structures like those reported in the literature[7] for growth of this iron oxide phase, but some of our films have the perfectly smooth surface termination when imaged with SEM. Most of the SEM images of the Fe_3O_4 films indicate an "orange peel" roughness of the surface with a grain size of several hundred angstroms. Growth of iron oxide films at significantly lower temperature than our standard substrate temperature of 240 °C showed the presence of rings in the RHEED electron diffraction pattern as well as low-intensity diffraction lines in the XRD data indicative of multiphase formation and polycrystallinity in the oxide growth. SEM images of such film surfaces indicate large surface irregularities and the presence of crystallites several micrometers in size and larger.

Multiple-phase formation and formation of phase with oxygen stoichiometry different from Fe_3O_4 in the iron oxide growth are of potentially real concern, for a variety of stable oxide phases that have been observed under a variety of growth conditions.[4,7,10,12] Each of these phases have structural, magnetic, and transport characteristics that would be distinctly different from Fe_3O_4, but XRD or RHEED data indicate no evidence for other phases in our films. One of the potential competing phases, γ-Fe_2O_3, is of special concern because it has a cubic spinel crystal structure with unit-cell dimensions (8.34 Å) very near that of Fe_3O_4 (8.397 Å), and which also has a small (0.93%) lattice mismatch for pseudomorphic growth on MgO. Clearly, the problem with competing phases is that they often have structures that very nearly match the desired phase. However, the lattice constant of the γ-Fe_2O_3 phase is different enough from either the measured lattice constant of our films or the unstrained lattice constant of bulk crystalline Fe_3O_4 that forced growth of γ-Fe_2O_3 under the conditions observed for our films would cause it to have a Poisson ratio greater than 1.0, which is felt to be very unlikely. While some Fe vacancies, leading to a somewhat more "γ-Fe_2O_3-like" material, may be present in our films and superlattices, the measured properties of our films are predominantly "Fe_3O_4-like."

Both electron transport and magnetization data taken on our films support the formation of the single phase—Fe_3O_4. Magnetization measurements[13] show saturation magnetization and coercive fields especially in the longer modulation wavelength superlattices that are consistent with Fe_3O_4 phase formation, but the saturation moment is greater than, and the magnetic hysteresis behavior is different from, that measured elsewhere for γ-Fe_2O_3. In addition, electron transport measurements[14,15] on our iron oxide thin films show the proper low-temperature electrical conductivity, including the Verwey transition near 120 K, which is characteristic of Fe_3O_4, but are not observed in the other iron oxide phases.[31,31] Furthermore, the electron-transport data in the short-wavelength superlattices indicate that the in-plane electron conductivity is primarily "Fe_3O_4-like," having the proper magnitude and temperature dependence for that phase but far too high conductivity to be consistent with "γ-Fe_2O_3-like" phase formation. However, in these short modulation wavelength superlattices, the Verwey transition that was observed in the thick Fe_3O_4 films is not observed. We believe that the Verwey transition, which accompanies an orthorhombic lattice distortion, may be locked out of the thin superlattice Fe_3O_4 layers by large local strain. Our studies thus indicate that Fe_3O_4 phase stability is maintained into the superlattices as well, although there is some evidence that the shorter modulation wavelength superlattices have a lattice constant shifted enough so that the presence of some "γ-Fe_2O_3-like" phase cannot be ruled out.

Also shown in Fig. 4(d) is the θ-2θ diffraction pattern for a superlattice composed of Fe_3O_4 and NiO layers grown with a repeat wavelength $\Lambda=64.76$ Å, namely Fe_3O_4 and NiO layer thicknesses of 29.40 and 35.36 Å, respectively, with a total of 131 repeats of each. Hereafter we label our superlattices by the thickness of the Fe_3O_4 layer divided by the thickness of the NiO layer, to the nearest angstrom: [e.g., Fe_3O_4(29 Å)/NiO(35 Å) for the above superlattice]. The entire diffraction pattern revealed peaks at $2\theta=43.379°$ and 95.319° corresponding to an interatomic layer spacing in the film of 2.0834 Å. We will denote these interatomic layer spacing peaks by (004),(002) and (008),(004).[27] Note that the lattice spacing measured for this film does not fall between the measured layer spacings of the two constituent materials grown as separate films. Clearly, strain in the thin layered structure must play a role in this shift in the film's normal lattice spacing.

In addition to a shift in lattice parameter observed for the superlattices, there is also a lowering in the uniformity in the lattice spacing in these strained layered systems, and it is seen as a broadening in the diffraction linewidths. The interatomic layer spacing in lattice-mismatched structures is always found to vary with composition, due to interfacial strain. The 2θ-rocking curve linewidth is a reflection of this variation in lattice spacings, and may be used to quantify the strain in the grown

layered structure. The 2θ-rocking curve linewidth for the Fe_3O_4(29 Å)/NiO(35 Å) superlattice (004),(002) peak at $2\theta=43.3°$ is (FWHM) 0.095°, which corresponds to a variation in lattice spacings of ±0.0021 Å, or 0.10% of the interlayer spacing.

In Fig. 4(d), the +1 and −1 superlattice sidebands on either side of the superlattice (008),(004) peak are visible with the +1 sideband observable as a sharp $K\alpha_{1,2}$ doublet. It should be noted that for most of the superlattices measured the sidebands on either side of this (008),(004) central peak are generally weak, with between two and four sidebands visible on the high-angle (+) side and often either one or two visible on the low-angle (−) side. This is not the case for the sidebands that accompany the superlattice (004),(002) diffraction feature, where a large number of sidebands on either side of the central peak are generally observed.

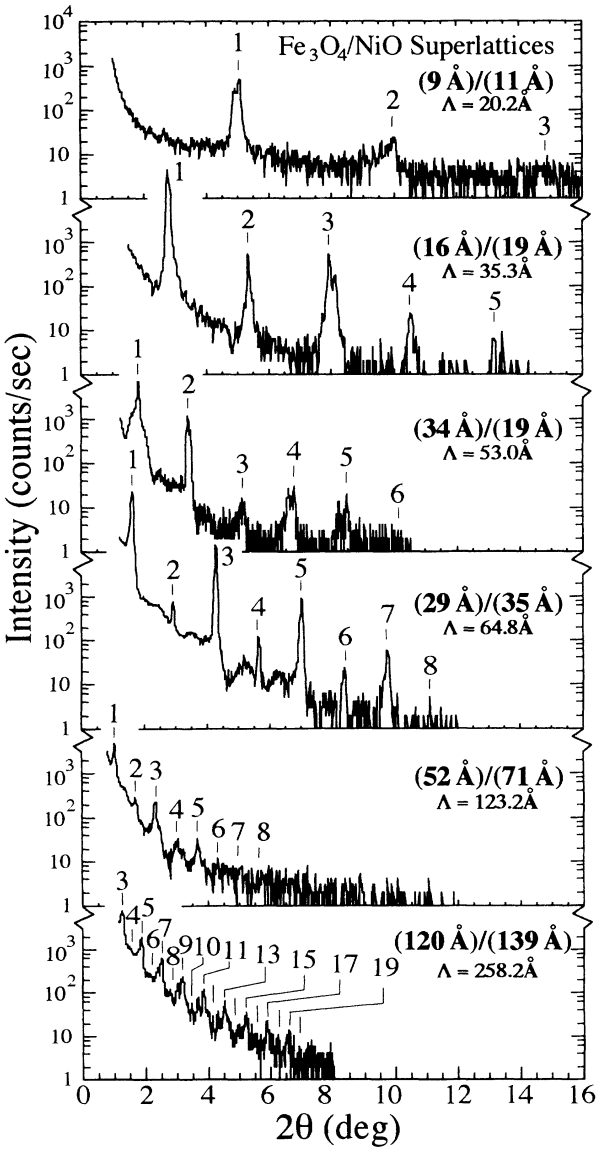

FIG. 5. X-ray diffraction spectra from superlattices with modulation wavelengths between Λ=20.1 and 258.2 Å. Shown is the near-glancing-incidence low angular range.

Shown in Figs. 5 and 6 are the diffraction spectra at low and intermediate angles for superlattices of Fe_3O_4/NiO with modulation wavelengths in the range from 20.15 to 258.15 Å. The diffraction spectra shown in Fig. 5 are comprised of the angular range at grazing incidence near 0°, and those in Fig. 6 are for the angular range around the (004),(002) (Ref. 27) superlattice interlayer spacing diffraction feature near $2\theta=43.3°$. Observable are many superlattice sidebands reflective of the modulation wavelengths of the superlattices. Each of the films was grown with nominally equal Fe_3O_4 and NiO layers (resulting in actual relative layer thicknesses having ratios near 45% Fe_3O_4 and 55% NiO), with each superlattice in the sequence having approximately twice the modulation wavelength (and component layer

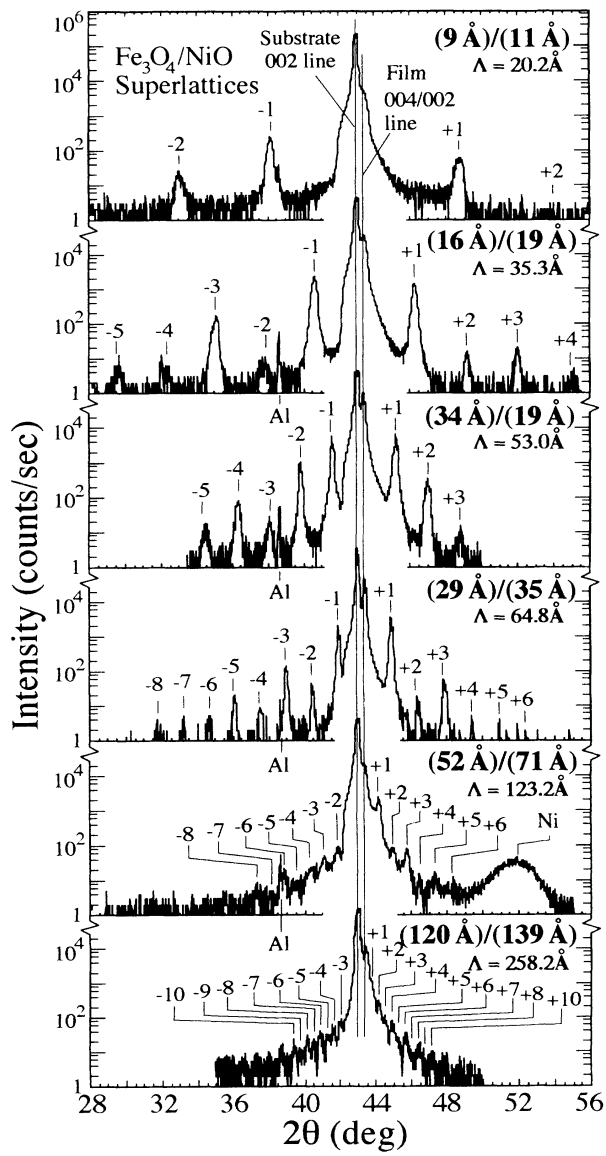

FIG. 6. X-ray diffraction spectra from superlattices with modulation wavelengths between Λ=20.1 and 258.2 Å. Medium angular range. The central diffraction peak for the superlattices is (004),(002), the MgO substrates diffraction peak is (002), and both are indicated by thin vertical lines near 43°.

thicknesses) as the one preceding it. The one significant deviation from this rule is the Fe_3O_4(34 Å)/NiO(19 Å) film which was grown to have Fe_3O_4 layers nominally twice as thick as the NiO layers. The relative atomic percents of Fe and Ni, and therefore the relative layer thicknesses compensated for density, are set by the shuttering times of each source opening during superlattice deposition, and are confirmed using energy dispersive x-ray spectra compared against known oxide standards during scanning electron microscopy.

On both the high- and low-angle sides of each of the "interatomic layer spacing" diffraction peaks, a number of superlattice satellite peaks are seen. These sideband peaks are a reflection of the modulation of both the chemical composition and of the interatomic layer spacing with alternation of the two components in the superlattices. Analysis of the superlattice sideband peak intensities must account for both of these contributions.

Superlattice satellite peaks are also seen at very low grazing angle (near the straight-through undiffracted incident x-ray beam). The position and intensity of these low-angle diffraction peaks are insensitive to modulation in lattice spacing, and are more sensitive to the chemical modulation. The diffraction data are shown plotted on a logarithmic scale to present more clearly the small superlattice satellite sideband peaks. At least five, and sometimes many more, superlattice sidebands are seen on either side of each central peak or alongside the straight-through beam. The only exception to this rule is for the very shortest wavelength Fe_5O_4(9 Å)/NiO(11 Å) superlattice, which has very widely spaced lines, and for which only three peaks are seen.

Analysis of the superlattice satellite peak positions is used to obtain the modulation wavelength in the following manner: The peak positions of each of the satellite peaks are obtained and their values θ_{meas} are fit using

$$\frac{2\sin(\theta_{meas})}{\lambda}=\frac{l}{a}+\frac{m}{\Lambda},$$

where a is the interatomic layer spacing for the film obtained from the position of the superlattice atomic interlayer spacing peak, λ is the x-ray radiation wavelength, Λ is the superlattice modulation wavelength, l is the order of diffraction of the interlayer d spacing (0 for "through" beam, 1 and 2 for diffraction peaks), and m is the order of the superlattice satellites on either side of each diffracted peak ($\pm1,\pm2,\pm3,\ldots$). In several cases, the values of Λ obtained from the $l=0,1,2$ derived sidebands differ by an amount substantially exceeding the experimental uncertainties. We have no explanation for this unexpected behavior. The structural results for several of our Fe_3O_4/NiO thin films and superlattices, taken primarily from $l=1$ data, are given in Table I.

The interatomic layer spacing or lattice parameter within the superlattice structure may be measured directly from the position of the central diffraction features. But because small inaccuracies in sample positioning in the x-ray diffractometer could affect the derived lattice spacing, a more accurate measure of the variation in lattice constant with superlattice modulation wavelength is the fractional difference between the lattice spacings measured for the film and substrate in the same data scan from angular measurements immediately beside one another. This variation in the lattice parameter with modulation wavelength, which is shown as $\Delta a/a$ plotted against Λ in Fig. 7, is a very sensitive gauge of the lattice mismatch, and thus also of elastic strain, for the various films. The shift in lattice d spacing, $\Delta a/a$, is given by

$$\frac{a_{SL}-a_{sub}}{a_{sub}}=\frac{\Delta a}{a},$$

where a_{sub} is the substrate interatomic layer spacing and a_{SL} is the superlattice interatomic layer spacing, each normal to the film plane, as measured by XRD. The markings on the right-hand side of the graph (Fig. 7) indicate the $\Delta a/a$ values obtained for our pure Fe_3O_4 and NiO films grown on MgO, and for bulk Fe_3O_4 and NiO from JCPDS–International Centre for Diffraction Data[17] when compared to the lattice constant of MgO. The bulklike JCPDS values give the unstrained cubic lattice spacings of the constituent NiO and Fe_3O_4 layers, and the film values give the lattice spacings when the strain con-

TABLE I. Experimentally derived structural parameters of superlattices and thin films. All lengths shown in the table are in angstroms unless otherwise noted. The relative layer thicknesses of the Fe_3O_4 and NiO are set during growth by layer thickness settings and confirmed using the atomic concentration ratios obtained in quantitative dispersive x-ray analysis during scanning electron microscopy.

Nominal layer-thickness ratio	Fe_3O_4-layer thickness (Å)	NiO-layer thickness (Å)	Number of bilayer repeats	Repeat wavelength Λ (Å)	Total thickness	Film interatomic spacing a_{SL} (Å)	Substrate interatomic spacing a_{sub} (Å)	Lattice mismatch (%)
MgO substrate					0.5 mm		2.1048	
Fe_3O_4 layer					10 300	2.0935	2.1057	−0.582
NiO layer					8 000	2.0883	2.1051	−0.806
(9 Å)/(11 Å)	8.9	11.3	300	20.15	6 050	2.0855	2.1059	−0.976
(16 Å)/(19 Å)	16.1	19.1	120	35.27	4 250	0.0821	2.1034	−1.019
(34 Å)/(19 Å)	33.7	19.3	111	53.02	5 880	2.0875	2.1063	−0.901
(29 Å)/(35 Å)	29.4	35.4	131	64.77	8 480	2.0843	2.1038	−0.936
(42 Å)/(33 Å)	41.6	33.1	150	74.78	11 300	2.0883	2.1049	−0.795
(52 Å)/(71 Å)	52.0	71.2	80	123.19	10 040	2.0889	2.1039	−0.717
(120 Å)/(139 Å)	119.6	138.5	45	258.15	11 620	2.0895	2.1048	−0.732

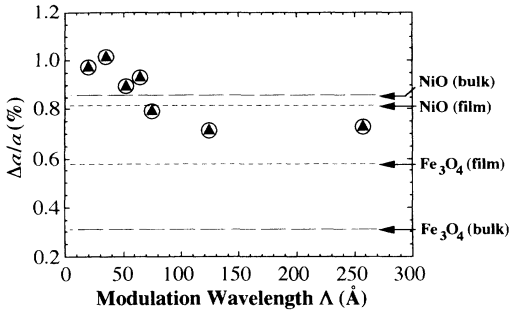

FIG. 7. Interlayer spacing mismatch (between superlattice and substrate) vs superlattice modulation wavelength. See text for discussion.

tributed by the film-substrate interface coupling is included. Note the following: (1) If the modulated structures grown here are composed of a composite of elastically matched slabs of equal thickness, and includes coupling to the substrate, then the $\Delta a/a$ should fall halfway between the measured film values for Fe_3O_4 and NiO on MgO, or $\sim 0.7\%$, and that this should be true for all Λ. (2) If, on the other hand, the modulated structure components are bulklike, elastically matched, and elastically decoupled from the substrate, $\Delta a/a$ should full halfway between the bulk values for Fe_3O_4 and NiO, here $\sim 0.6\%$, and once again independent of Λ. Clearly the equilibrium elastic parameter for the modulated structures, especially for the short modulation wavelength superlattices, has large variation from the macroscopic bulklike behavior, and a simple elastic model does not completely describe the lattice mismatch found in this type of strongly coupled material.

X-ray 2θ-rocking curve data taken on the superlattice sidebands provide supporting evidence for a higher degree of coherence in the short modulation wavelength superlattices. The 2θ-rocking curve data, which are a measure of the uniformity of the modulation wavelength Λ throughout the film, show the sidebands of the short-wavelength superlattices to have narrower 2θ FWHM linewidths and, thus, better uniformity in modulation wavelength than the longer wavelength superlattices. Generally, however, the modulation wavelength uniformity for all superlattice is measured to be $\leq \pm 1.0$ Å, which is felt to be quite good.

The presence of many orders of superlattice sidebands, observable for essentially all of our grown modulated structures, is a clear indication of the abruptness of the chemical and spacing modulation in the superlattice structure in these materials. The occurrence of both odd and even order sidebands, with the former being larger, is very consistent with a one-dimensional Fourier transform model for modulated structures with nearly square wave modulation and nearly equal layer thicknesses. Such a model is inconsistent, however, with significant interdiffusion between the chemically different layers. During the growth of our superlattices, we have made no attempt at terminating the deposition of each material at the completion of an integral number of atomic layers. As a result, even for perfectly uniform layer-by-layer growth, the surface will be covered with single-layer-height island—effectively one layer's thickness worth of surface roughness. As this surface is then deposited upon, an *interfacial* roughness, equivalent to a single atomic layer's worth of interdiffusion, will be left behind. The large number of superlattice sidebands, and the narrowness of their measured rocking curve widths, is inconsistent with significantly more interdiffusion than would be accounted for by this level of interfacial roughness.

We have performed Fourier analysis on our x-ray data to obtain an estimate of the thickness of the transition region between the iron oxide and nickel oxide layers within our modulated structures. We assumed for this analysis that the crystal is an ideal one-dimensional solid and that the x-ray diffraction pattern is a function of only the modulation of electron density within the layered structure. That electron density can be obtained by the inversion of the x-ray diffraction data by properly scaling and then taking the Fourier transform. Such a simplified analysis indicates that the structure and electron density within the iron oxide layers are consistent with the layer projected density of a spinel ferrite of Fe_3O_4 structure, and that the comparable density within the nickel oxide layers is consistent with the rocksalt structure. Furthermore, the analysis shows that over a boundary of less than 2–3 atomic layers the electron density transitions from that of the one material completely to that of the other, indicating that interdiffusion between the Fe_3O_4 and NiO layers in our films is of the order of 1 or 2 atomic layers thickness. A continued, more detailed analysis of the interfacial coherence and interdiffusion of our superlattices, using aspects of the techniques used by Fullerton *et al.*,[32] Guinier,[33] and McWhan and coworkers,[34,35] and taking into account the structural and atomic scattering factors in the x-ray diffraction, and of details of the compositional modulation on the intensities of the superlattice sidebands, is in progress at this time.

The surfaces of the short modulation wavelength ($\Lambda \leq 65$ Å) superlattices are found to be very smooth and featureless—apparently atomically flat—down to highest resolution in SEM images, and show sharp cubic cleavage aligned along {100} planes of the substrate and extending all the way through the grown film. Clearly, the grown materials have highly ordered crystalline structures of overall cubic symmetry which is well aligned with the substrate. The evidence also seems to indicate that the superlattices that have the highest degree of crystalline coherence are the superlattices that exhibit the highest degree of interplanar strain. Flynn[36,37] and van der Merwe[28] both comment on this phenomenon, and note that strain may assist the epitaxial growth process. The longer-wavelength superlattices, where lattice mismatch and strain are lower, appear under SEM to be more "like" their constituent layers, and the Fe_3O_4(120 Å)/NiO(139 Å) superlattice [and to a lesser extent the Fe_3O_4(52 Å)/NiO(71 Å) superlattice] shows a rough surface topography similar to those seen in many of the Fe_3O_4 films, while the shorter modulation wavelength superlattice surfaces are very smooth.

In addition to those thin films discussed above, we have

also grown NiO and Fe_3O_4 films on other dissimilarly prepared substrates, and we will discuss them briefly here. Fe_3O_4 and NiO thin films and modulated structures have been grown on MgO(001) samples that were cleaved in air immediately before introduction into the vacuum chamber and on the (0001) cleavage plane of mica, often with a buffer layer of Ni and/or NiO. These latter samples were used to perform a range of electron transport studies. Studies of the films grown on the cleaved MgO substrates using XRD, RHEED diffraction, SEM, profilometry, and optical microscopy indicate that growth takes place on substrate cleavage terraces which are approximately 10–50 μm across with a growth mode identical to that on the polished substrates. MgO is quite a hard material, and is difficult to cleave into thin enough samples so that the inherent diamagnetism of the substrates does not overwhelm the measured magnetic moments of the thin (≤ 1 μm) films in subsequent magnetization studies. As a result the commercial polished substrates were used for most of the detailed studies presented here. Interestingly, however, the commercially obtained MgO substrates, which are epitaxially grown themselves, contain V centers—Mg vacancy sites within the lattice—which show up as a paramagnetic contribution in the magnetization studies and, thus, also must be accounted for. The cleaved MgO substrates, obtained from Dr. Lynn Boatner at Oak Ridge National Laboratory as a single ingot, show no evidence for the presence of V centers.

The oxide thin film deposition on Ni-coated mica substrates showed somewhat different growth patterns. X-ray diffraction studies indicate that Fe_3O_4 and NiO thin films and modulated structures, grown on the Ni-coated mica substrates are highly oriented but polycrystalline, with the largest contribution to the film interatomic layer intensities having (111) and (001) crystallographic orientation aligned with the surface normal. The (001) diffraction lines comprise $\sim 60\%$ of the total integrated x-ray intensity from the films. Superlattice satellite sidebands similar to those described above for superlattices on MgO are observed in x-ray diffraction from the Fe_3O_4/NiO modulated structures grown on Ni-coated mica, and are found indexed off of the observed (222),(111) and (004),(002) (Ref. 27) diffraction lines. Usually superlattice sidebands up to 2–3 orders on either side of the central peak are identifiable for each (222),(111) or (004),(002) line.

In conclusion, our work has shown that highly oriented single-crystalline thin films of NiO, Fe_3O_4; and Fe_3O_4/NiO superlattices can be grown on MgO(001), using oxygen-plasma-assisted molecular-beam epitaxy. We have presented the techniques used in this film synthesis, and have shown how the grown films have been structurally characterized using reflection high-energy electron diffraction, scanning electron microscopy, and x-ray diffraction. We found the (001) surface of MgO to provide an excellent template for the pseudomorphic growth of both NiO and Fe_3O_4 due to its small ($< 1\%$) lattice mismatch to the cubic rocksalt structure of the former, and to the half unit-cell dimension of the spinel structure of the latter. We described the preparation of NiO and Fe_3O_4 thin films, as well as superlattices consisting of alternating layers of NiO and Fe_3O. The Fe_3O_4/NiO superlattices have been grown with modulation wavelength Λ between 20 and 258 Å (the lower limit being slightly greater than one Fe_3O_4 unit cell plus two NiO unit cells) thick, with optimal crystalline order obtained at substrate growth temperature of 240 °C. These films exhibit coherent single-crystalline ordering over several hundred repeat wavelengths. Reported elsewhere in the literature are studies of the magnetization and electron transport properties of these thin films and superlattices.[13–15]

ACKNOWLEDGMENTS

We would like to acknowledge the contributions of Lynn Boatner, ORNL, for the donation of high quality single-crystal MgO substrates; to W. G. Moulton and E. Manousakis for a number of useful discussions; to Ed Clark, for his contribution to some of the early growths and calibration of the substrate heater; and to Tom Fellers for his technical expertise in scanning electron microscopy.

[1] *Materials Science and Engineering for the 1990s,* edited by Praveen Chaudhari and Mertin Flemings, Committee on Materials Science and Engineering, National Research Council (National Academy Press, Washington, D.C., 1989).

[2] For excellent reviews, see L. M. Falicov, D. T. Pierce, S. D. Bader, R. Gronsky, K. B. Hathaway, H. J. Hopster, D. N. Lambeth, S. S. P. Parkin, G. A. Prinz, M. Salamon, I. K. Schuller, and R. H. Victora, J. Mater. Res. **5**, 1299 (1990); E. G. Bauer, B. W. Dodson, D. J. Ehrlich, L. C. Feldman, C. P. Flynn, M. W. Geis, J. P. Harbison, R. J. Matyi, P. S. Peercy, P. M. Petroff, J. M. Phillips, G. B. Stringfellow, and A. Zangwill, *ibid.* **5**, 852 (1990), and references cited therein.

[3] G. A. Prinz, Science **250**, 1092 (1990).

[4] T. Shigematsu, H. Ushigome, Y. Bando, and T. Takada, J. Cryst. Growth **50**, 801 (1980).

[5] T. Terashima and Y. Bando, J. Appl. Phys. **56**, 3445 (1984).

[6] T. Terashima and Y. Bando, Thin Solid Films **152**, 455 (1987).

[7] T. Fujii, M. Takano, R. Katano, Y. Bando, and Y. Isozumi, J. Appl. Phys. **66**, 3168 (1989), and references cited therein.

[8] T. Fujii, M. Takano, R. Katano, Y. Bando, and Y. Isozumi, J. Appl. Phys. **68**, 1735 (1990).

[9] T. Fujii, M. Takano, R. Katano, Y. Bando, and Y. Isozumi, J. Cryst. Growth **99**, 606 (1990).

[10] C. Ortiz, G. Lim, M. M. Chen, and G. Castillo, J. Mater. Res. **3**, 344 (1988).

[11] C. Ortiz, C. Hwang, A. H. Morish, and X. Z. Zhou, J. Mater. Res. **5**, 824 (1990).

[12] S. Yoshii, O. Ishii, S. Hattori, T. Nakagawa, and G. Ishida, J. Appl. Phys. **53**, 2556 (1982).

[13] D. M. Lind, S. D. Berry, G. Chern, H. Mathias, and L. R. Testardi, J. Appl. Phys. **70**, 6218 (1991).

[14] G. Chern, S. D. Berry, D. M. Lind, H. Mathias, and L. R.

Testardi, Appl. Phys. Lett. **58**, 2512 (1991).

[15]S. D. Berry, D. M. Lind, G. Chern, H. Mathias, and L. R. Testardi (unpublished); G. Chern, S. D. Berry, D. M. Lind, H. Mathias, and L. R. Testardi, Phys. Rev. B (to be published).

[16]For the structure of oxide spinels and its influence on the magnetic ordering in this class of materials, including Fe_3O_4, see the excellent discussion by S. Chikazumi, *Physics of Magnetism* (Wiley, New York, 1964).

[17]*Powder Diffraction File: Inorganic Phases,* edited by W. F. McClung (International Centre for Diffraction Data, Swarthmore, PA, 1990).

[18]J. W. Matthews, in *Physics of Thin Film: Advances in Research and Development,* edited by Georg Hass and Rudolf E. Thun (Academic, New York, 1967), Vol. 4.

[19]J. W. Matthews, in *Epitaxial Growth* edited by J. W. Matthews (Academic, New York, 1975), Pt. B.

[20]A. Kobayashi and S. Das Sarma, Phys. Rev. B **35**, 8042 (1987).

[21]Fabricated by EPI Systems, Inc. St. Paul, MN.

[22]Coating & Crystal Technology, Inc., Kittaning, PA.

[23]Atlantic Equip. Eng., Inc. Bergenfield, NJ.

[24]See M. A. Herman and H. Sitter, *Molecular Beam Epitaxy* (Springer-Verlag, Berlin, 1989); B. D. Cullity, *Elements of X-Ray Diffraction,* 2nd ed. (Addison-Wesley, Reading, MA, 1978), and references cited therein.

[25]A. Segmüller and A. E. Blakeslee, J. Appl. Cryst. **6**, 19 (1973).

[26]B. Y. Jin and J. B. Ketterson, *Advances in Physics, 1989* (Taylor & Francis, New York, 1989), Vol. 38(3), pp. 189–366, and references cited therein.

[27]The order of the Fe_3O_4 diffraction peaks observed near $2\theta=43.2°$ and 94.7° are (004) and (008) due to the longer unit-cell dimensions in the spinel, compared to the other latices. This leads to an ambiguity in the nomenclature for the interlayer diffraction features for d spacings in the superlattices. Because the interlayer spacings indexed by these diffraction features contain both the d_{004} [or d_{008}] character of Fe_3O_4 and the d_{002} [or d_{004}] character of NiO, we will label the central (i.e., interlayer spacing) diffraction features observed for the superlattice interlayer spacings by (004),(002) [and (008),(004)].

[28]J. H. van der Merwe, in *Chemistry and Physics of Solid Surfaces V,* edited by R. Vanselow and R. Howe (Spinger, Berlin, 1984), and references cited therein.

[29]See also E. Bauer, Appl. Surf. Sci. **11/12**, 475 (1981).

[30]E. J. T. Verwey, *Semi-conducting Materials* (Butterworth, London, 1951).

[31]*Handbook of Physics,* 1st ed., edited by E. U. Condon and Hugh Odishaw (McGraw-Hill, New York, 1958), pp. 80–83.

[32]E. E. Fullerton, I. K. Schuller, H. Vanderstraeten, and Y. Bruynseraede (unpublished).

[33]A. Guinier, *X-Ray Diffraction in Crystals, Imperfect Crystals, and Amorphous Bodies,* translated by P. Lorrain and D. Sainte-Marie Lorrain (Freeman, San Fransisco, 1963), pp. 279–282.

[34]D. B. McWhan, M. Gurvitch, J. M. Rowell, and L. R. Walker, J. Appl. Phys. **54**, 3886 (1983).

[35]R. M. Fleming, D. B. McWhan, A. C. Gossard, W. Wiegmann, and R. A. Logan, J. Appl. Phys. **51**, 357 (1980).

[36]C. P. Flynn, Phys. Rev. Lett. **57**, 599 (1986).

[37]See also J. L. Martins and A. Zunger, Phys. Rev. Lett. **56**, 1400 (1986).

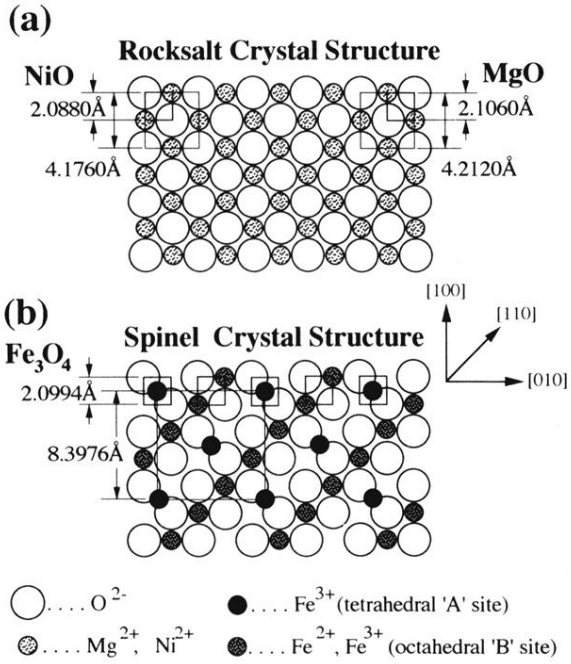

FIG. 1. The surface net of the (001) face of NiO, MgO, and Fe_3O_4. The overall symmetry is that of a face-centered-cubic oxygen lattice with metal ions coordinated around the oxygen sites. The spinel structure has two different Fe coordination sites, either octahedrally and tetrahedrally coordinated about alternating oxygen sites. The tetrahedrally coordinated sites shown lie $\frac{1}{2}$ lattice plane in front of the plane in which the rest of the atoms lie. The MgO and NiO structures have the NaCl (rocksalt) -structure crystal symmetry.

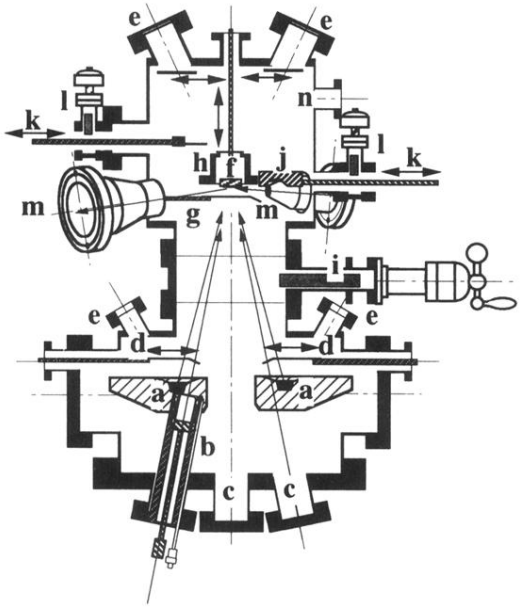

FIG. 2. Ultrahigh vacuum molecular-beam epitaxy (MBE) thin-film growth chamber. The deposition sources are in the lower chamber facing upward and include two 15-kW electron-gun sources (*a*), an ECR magnetically focused gas plasma source (*b*) with gas inlet, and four Knudsen effusion sources [not shown (*c*)], with all sources pneumatically shuttered (*d*), and source charges visible from shuttered viewports (*e*). The substrate holder (*f*) is shuttered (*g*) and placed in a heating shroud (*h*) in the upper chamber. The chambers are joined by an 8.0-in. i.d. isolation gate valve (*i*). Both quartz crystal deposition rate monitor head (*j*) and the substrate holder (*f*) may be retracted (*k*) and gated (*l*) from the main chamber for replacement. Grazing incidence RHEED diffraction (*m*), and quadrapole residual gas analysis (*n*) are also available in the upper chamber.

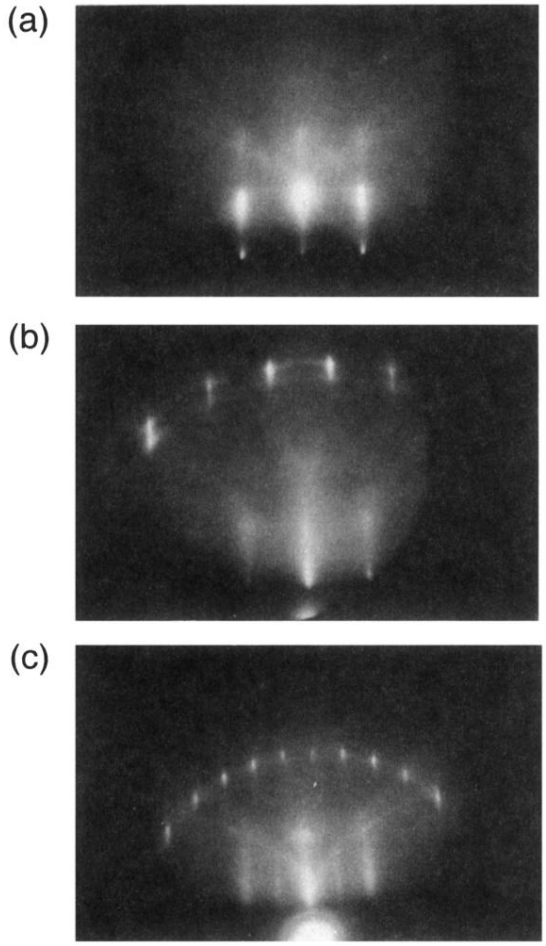

FIG. 3. RHEED images of (a) MgO(001), (b) NiO/MgO(001), and (c) Fe_3O_4/MgO(001), taken at 10 kV along a ⟨100⟩ azimuth. The images are seen as though scattering off a crystal facing upward. See text for discussion.